The Relationships among Wind, Horizontal Pressure Gradient, and Turbulent Momentum Transport during CASES-99

Jielun Sun and Donald H. Lenschow

National Center for Atmospheric Research, Boulder, Colorado

Larry Mahrt

Oregon State University, Corvallis, Oregon

Carmen Nappo

CJN Research Meteorology, Knoxville, Tennessee

ABSTRACT

Relationships among the horizontal pressure gradient, the Coriolis force, and the vertical momentum transport by turbulent fluxes are investigated using data collected from the 1999 Cooperative Atmosphere–Surface Exchange Study (CASES-99). Wind toward higher pressure (WTHP) adjacent to the ground occurred about 50% of the time. For wind speed at 5 m above the ground stronger than 5 m s^{-1}, WTHP occurred about 20% of the time. Focusing on these moderate to strong wind cases only, relationships among horizontal pressure gradients, Coriolis force, and vertical turbulent transport in the momentum balance are investigated. The magnitude of the downward turbulent momentum flux consistently increases with height under moderate to strong winds, which results in the vertical convergence of the momentum flux and thus provides a momentum source and allows WTHP.

In the along-wind direction, the horizontal pressure gradient is observed to be well correlated with the quadratic wind speed, which is demonstrated to be an approximate balance between the horizontal pressure gradient and the vertical convergence of the turbulent momentum flux. That is, antitriptic balance occurs in the along-wind direction when the wind is toward higher pressure. In the crosswind direction, the pressure gradient varies approximately linearly with wind speed and opposes the Coriolis force, suggesting the importance of the Coriolis force and approximate geotriptic balance of the airflow. A simple one-dimensional planetary boundary layer eddy diffusivity model demonstrates the possibility of wind directed toward higher pressure for a baroclinic boundary layer and the contribution of the vertical turbulent momentum flux to this phenomenon.

1. Introduction

The horizontal pressure gradient is commonly thought to drive the atmospheric circulation. Its magnitude is typically about four orders of magnitude smaller than the vertical pressure gradient at the ground, which makes it difficult to measure on small scales. Small static pressure perturbations can result from the effects of turbulence, flow distortion induced by nearby structures, or the pressure probes themselves. Accurate pressure measurements require estimating the effects of dynamic pressure fluctuations, the angle-of-attack sensitivity of pressure probes (Wilczak and Bedard 2004), and the sensitivity of microbarograph output to temperature variations (Cuxart et al. 2002). Various probes have been developed to minimize effects of dynamic pressure fluctuations (Nishiyama and Bedard 1991; Akyüz et al. 1991).

Observational studies of horizontal pressure gradients have concentrated on mesolows and mesohighs (e.g., Vescio and Johnson 1992; Johnson 2001; Adams-Selin and Johnson 2010). Fujita (1963) examined mesoscale pressure disturbances by converting time variation to spatial variation when considering mesoscale system development in a moving synoptic environment. This

Corresponding author address: Jielun Sun, National Center for Atmospheric Research, P.O. Box 3000, Boulder, CO 80307-3000.
E-mail: jsun@ucar.edu

technique has been applied to various studies of surface pressure patterns in relation to mesoscale convective systems (e.g., Vescio and Johnson 1992; Adams-Selin and Johnson 2010). LeMone et al. (1988) investigated the mesoscale horizontal pressure gradient under developing clouds using the Fujita method for aircraft and ground observations. Parish et al. (2007) also estimated mesoscale horizontal pressure gradients from aircraft static pressure and global positioning system measurements.

In addition to the familiar geostrophic balance, the role of horizontal pressure gradients in the momentum balance has also been considered for antitriptic and geotriptic balances. Antitriptic balance in the momentum equation was first defined by Jeffreys (1922) as a stationary atmospheric flow in a spatially varying pressure field where the horizontal pressure gradient balances the vertical turbulent momentum transport, which he called the internal friction term. He also suggested that antitriptic flow only occurs for spatial scales of disturbances smaller than $O(10^2\,\text{km})$, for which the Coriolis force can be neglected. Based on the assumption of constant eddy viscosity, he further suggested that the antitriptic wind is toward lower pressure and the land or sea breeze is an example of an antitriptic flow. Johnson (1966) proposed the term geotriptic balance by including the Coriolis force in addition to the horizontal pressure gradient and the vertical turbulent momentum flux transport. We note that inconsistent usage of antitriptic balance appears in the literature. Saucier (1955) and Schaefer and Doswell (1980), for example, used the term antitriptic balance for what Johnson calls geotriptic balance. Here we use Jeffreys's original definition of antitriptic balance.

Antitriptic and geotriptic flows are often used to qualitatively describe mesoscale flows. Some examples are flow in mountainous terrain (McKendry et al. 1986; Bell and Bosart 1988; Colle and Mass 1996; Mass and Steenburgh 2000), flow in sloped environments (Parish and Waight 1987), and flow near the equator (Raymond 1993). Bell and Bosart (1988) found that the surface synoptic winds were approximately opposite to the vertical divergence of the turbulent momentum flux, which they calculated as the residual of the momentum balance, and concluded that the momentum flux divergence is proportional to the surface drag. Similarly, Colle and Mass (1996) calculated the turbulent momentum flux as the residual of the momentum balance and also concluded that the vertical divergence of the turbulent momentum flux is a drag although the wind and the residual terms are not in the opposite direction everywhere in their study. Using the surface friction to represent the vertical divergence of the momentum flux, Macklin et al. (1988) investigated geotriptic balance for offshore flows. Interestingly, we have found little observational

documentation in the literature for antitriptic balance occurring on scales smaller than $O(10^2\,\text{km})$.

Often, the vertical momentum transfer by the turbulent flux in the momentum balance is simply called the surface friction, especially in simple numerical models where this term is approximately estimated as the difference between the surface drag and the near-zero turbulent momentum flux at the planetary boundary layer (PBL) top (Bernhardt 1983; Haltiner and Williams 1990). Under this assumption, the airflow has to be down the pressure gradient.

The unique observational dataset collected from the 1999 Cooperative Atmosphere–Surface Exchange Study (CASES-99) (Poulos et al. 2002) provides an opportunity to investigate relations among the horizontal pressure gradient, wind, and vertical turbulent momentum transport in the momentum balance on a horizontal scale of less than 1 km. However, because of observational uncertainties discussed in section 2, we are not in a position to examine how well the momentum balances in general. Yet, we are able to investigate the role of the horizontal pressure gradient and its variation with other terms in the momentum balance during CASES-99. The observations and the methodology of estimating the horizontal pressure gradient and the turbulent flux used in this study are described in section 2. In section 3, we investigate relationships among the horizontal pressure gradient, the vertical variation of the turbulent momentum flux, wind speed, and the Coriolis force with a focus on wind toward higher pressure (WTHP). We discuss the duration of the WTHP phenomenon, the observed conditions when wind is toward lower pressure (WTLP), and implications of this study for antitriptic and geotriptic balances in section 4. Section 5 is a summary.

2. Observations and analysis methods

a. Observations

All the instruments relevant to this study were described in Sun (2011) and Sun et al. (2012). We used the eight levels of three-dimensional sonic anemometer wind measurements on the 60-m tower, as well as the wind, pressure, and air temperature measurements at six 10-m-high satellite towers surrounding the 60-m tower (Fig. 1). The lowest sonic anemometer was moved from 1.5 to 0.5 m on 20 October. The actual positions of the six 10-m towers, which differ from the original plan described in Sun et al. (2002), are listed in Table 1, where x and y represent the distances from the 60-m tower in the east–west and north–south directions, respectively, and the elevation of each tower is relative to sea level. The uncertainty of the station elevation is discussed in section 2c.
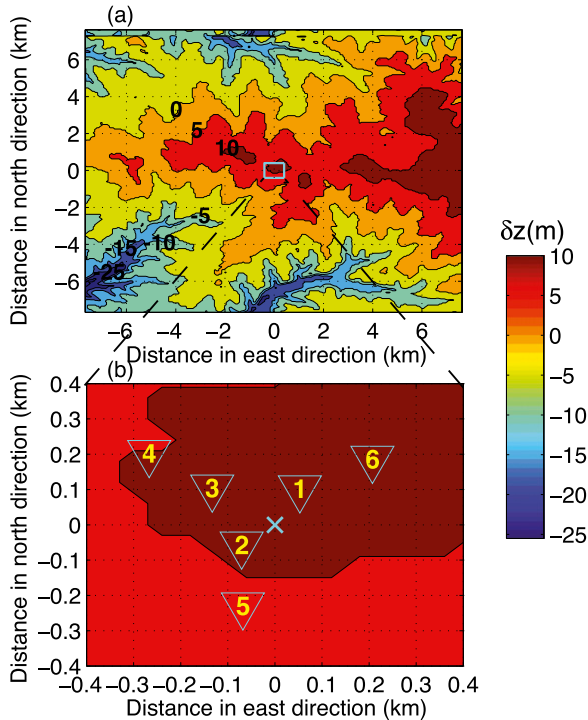
FIG. 1. (a) Contour map of the area centered on the CASES-99 60-m tower. (b) The blue box in (a), which includes all the CASES-99 towers, is enlarged. The numbers and the cross in (b) mark the station numbers and the 60-m tower, respectively. The numbers in (a) mark the contour values of the elevation relative to the area mean. The horizontal spatial resolution of the dataset is 60 m.

TABLE 1. The locations of the six satellite towers.

Station No.	Latitude (°)	Longitude (°)	Elevation (m)	x (m)	y (m)
1	37.648 93	−96.735 07	435.9	52.9	103.5
2	37.647 50	−96.736 47	433.6	−70.5	−55.7
3	37.648 95	−96.737 18	431.8	−133.1	105.8
4	37.649 83	−96.738 70	435.9	−267.1	203.7
5	37.645 95	−96.736 44	433.4	−67.9	−228.2
6	37.649 68	−96.733 32	438.6	207.2	187

b. Pressure measurements

During CASES-99, six identical pressure sensors were deployed at 1.5 m above the ground on the six satellite towers. Each pressure sensor consists of a Vaisala PTB220B transducer and a round disk port with asymmetric edges on two sides developed by the Earth Observatory Laboratory (EOL) at the National Center for Atmospheric Research (NCAR). The performance of the pressure sensor depends on the transducer error and the magnitude of dynamic pressure fluctuations induced by the pressure port. The design of the disk port minimizes dynamic pressure fluctuations due to the airflow attack angle relative to the disk, which are proportional to wind speed squared. Based on the wind tunnel test described by Akyüz et al. (1991), the dynamic pressure error of the pressure port used during CASES-99 is less than 0.01 hPa if the standard deviation of the attack angle is less than 5°, the mean attack angle is less than 2°, and the wind speed is less than 10 m s^{-1} for the roughness of the CASES-99 site. These conditions were met during CASES-99.

The NCAR EOL conducted a laboratory calibration in 2013 that compared the readings from seven pressure transducers used during CASES-99 with the reading from a pressure transducer with accuracy traceable to the NIST standard at preset pressure values ranging from 785 to 845 hPa. The bias of each pressure transducer was removed based on the calibration prior to CASES-99, which was still applicable for the 2013 calibration. We did not detect any time drift of the transducer output over the 100-h period of the calibration. Based on the calibration dataset, we estimate that the transducers were calibrated to an accuracy of about 0.01 hPa for the 30-min-averaged pressure values from CASES-99.

c. Horizontal pressure differences

To obtain horizontal pressure differences, the pressure difference due to elevation differences between the towers needs to be removed. Integrating the hydrostatic equation and applying the ideal gas law, we obtain

$$\ln(\overline{p}^c / \overline{p}^o) = -\frac{g\delta z}{R_d \overline{T}_v}, \tag{1}$$

where p is the air pressure, the superscripts c and o denote the corrected and observed values, g is the gravity acceleration constant, δz is the vertical difference used in the elevation correction, R_d is the gas constant for dry air, $\overline{T}_v$ is the virtual temperature averaged over the layer δz, and the overbars represent 30-min averaging.

We use $\overline{T}_v$ estimated from the 2-m air temperature and humidity measurements at each tower with the known elevation differences between the towers to correct for the elevation. Assuming an error $\delta \overline{T}_v$, its impact on $\overline{p}^c$ introduces an error $\delta \overline{p}^c$. Based on (1),

$$\delta \overline{p}^c = \overline{p}^o \left(\frac{g \delta z \delta \overline{T}_v}{R_d \overline{T}_v^2} \right) \exp\left(-\frac{g \delta z}{R_d \overline{T}_v} \right). \tag{2}$$

If $\overline{p}^o = 900$ hPa, $\delta z = 1$ m, $\overline{T}_v = 300$ K, and $\delta \overline{T}_v = 1$ K, the uncertainty in the corrected pressure is less than 4×10^{-4} hPa.

Assuming $(\overline{p}^c - \overline{p}^o)/\overline{p}^o \lesssim O(10^{-1})$, (1) can be approximated as

$$\ln(\overline{p}^c/\overline{p}^o) = \ln\left(1 + \frac{\overline{p}^c - \overline{p}^o}{\overline{p}^o}\right) \sim \frac{\overline{p}^c - \overline{p}^o}{\overline{p}^o} \sim -\frac{g\delta z}{R_d \overline{T}_v}. \tag{3}$$

Based on (3), if there is no horizontal pressure gradient over the CASES-99 domain of about 500 m $\times$ 500 m, and the air temperature and humidity are horizontally homogeneous, the measured pressure difference between the towers would be linearly proportional to the elevation difference between the towers. During a strong wind night of 17 October, $\overline{T}_v$ estimated from the measurements at 2 m was approximately the same at all the towers and within the lowest 8 m above the ground for about 2 h owing to the strong turbulent mixing close to the ground. The observed approximately linear relationship between the measured pressure difference and the elevation difference between the towers in Fig. 2 suggests that the estimated elevation is within the pressure measurement accuracy for stations 4 and 6. For the air temperature of 282 K during this period, the pressure varies with height by -0.12 hPa m^{-1}. Station 2 is 0.6 m off the line, which is the largest offset among all the stations except station 3 at a small-scale depression area. Using Fig. 2, we can estimate the elevation difference between the towers, which has an uncertainty of 0.08 m corresponding to the pressure uncertainty of 0.01 hPa. The absolute elevation of each station above sea level is irrelevant in the pressure difference calculation. Because the error introduced by the temperature uncertainty is relatively small, the error involved in the elevation correction is mainly from the elevation difference, which is systematic and does not affect relationships between the variation of the horizontal pressure gradient and other variables. Possible systematic biases of the pressure measurements due to the elevation uncertainty are further tested in section 3.

Using (3), the observed pressure at tower i is corrected relative to the elevation of tower j by

$$\overline{p}_i^c = \overline{p}_i^o\left[1 - \frac{g(z_j - z_i)}{R_d \overline{T}_{vi}}\right]. \tag{4}$$

To obtain the horizontal pressure gradient $\nabla\overline{p}$, we choose four satellite towers: two are closely aligned in the north–south direction (towers 2 and 5, separated by 172.5 m) and two in the east–west direction (towers 4 and 6, separated by 474.3 m). Based on Fig. 2, the elevation difference is less than 0.2 m between towers 2 and 5 and less than 2.8 m between towers 4 and 6.

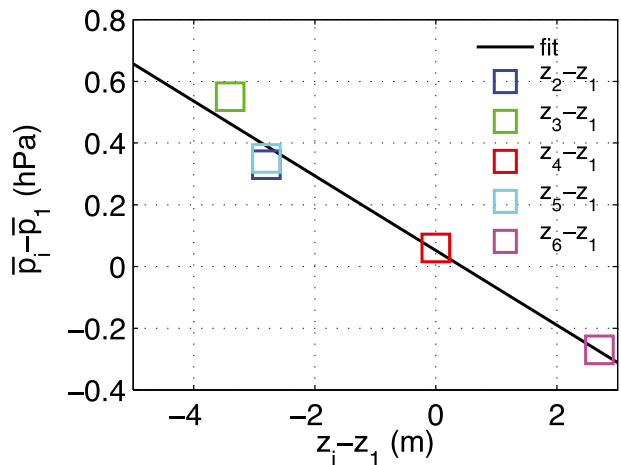The accuracy of pressure differences between two pressure sensors is theoretically between zero and

FIG. 2. The correlation between the elevation difference and the pressure difference between each tower (towers 2–6) and tower 1 for the windy night of 17 Oct when the surface air temperature was spatially homogeneous near the ground. The black line represents the fitted linear relationship.

$(\sigma_1^2 + \sigma_2^2)^{1/2}$, where σ_1 and σ_2 are the accuracies of sensors 1 and 2, depending on how well the fluctuations measured by the two sensors are correlated. If readings from the two sensors were identical for the same pressure variation, the accuracy of the pressure difference would be perfect. If readings from two sensors were not correlated at all, the accuracy of the pressure difference would be $(\sigma_1^2 + \sigma_2^2)^{1/2}$. Based on the NCAR EOL laboratory test, we find that the measurements between the sensors are highly correlated and the accuracy of the 30-min-averaged pressure differences remains around 0.01 hPa.

To calculate meaningful horizontal gradients of any variable, the accuracy of the measured difference is not the only concern. Another important issue is the relevant separation between observations for calculating horizontal gradients. If the separation is too large, the estimated gradient may not be relevant for the flow between the measurement locations. For example, the airflow may change directions in between in response to forcing on scales smaller than the separation. If the separation is too small, the sensitivity and accuracy of the instruments may not be good enough for estimating meaningful differences. A good example of investigating spatial variations of variables is reported by Staebler and Fitzjarrald (2004, 2005), who characterized subcanopy motions within the domain of their subcanopy-CO_2-advection study.

To ensure our estimated horizontal pressure gradient make sense in the momentum balance, we investigate how its variation is related to the other terms in the momentum balance. The relationship between the variation of the estimated horizontal pressure gradient and the other terms would be significantly scattered if the

horizontal pressure gradient is not related to the other terms in the momentum equation on the spatial scale of the pressure sensor separation even though the pressure sensor is sensitive enough to capture variations of horizontal pressure differences. Therefore, we utilize the relationship between the horizontal pressure gradient and other variables in the momentum balance to judge the accuracy of the pressure gradient estimate to complement our horizontal pressure gradient estimates.

The horizontal pressure gradient may also vary spatially within the observation domain. For example, the pressure gradients in x and y directions vary slightly depending on the stations used in estimating the horizontal pressure gradient. Both the largest horizontal pressure gradient and the strongest wind are in the north–south direction, so that the pressure gradient in the y direction calculated from stations 2 and 5 gives the largest horizontal pressure gradient close to the 60-m tower. Choosing different towers other than stations 4 and 6 to estimate $\partial \overline{p}/\partial x$ changes the direction of the horizontal pressure gradient slightly. But it does not affect the main conclusion in this paper as we mainly focus on moderate to strong winds (i.e., the wind speed at 5 m above the ground larger than $5\,\mathrm{m\,s^{-1}}$), for which the wind direction is well defined, the vertical variation of wind direction can be ignored, and, as discussed later, the flux uncertainty from intermittent submeso motions tends to be small.

To compare the horizontal pressure gradient from CASES-99 and independent pressure measurements about 56 km west of the CASES-99 site, we choose the strongest horizontal pressure gradient day: 15 October. The horizontal pressure gradient based on the surface measurements between two stations separated by about 20 km is on the same order of magnitude as the one from the CASES-99 site. In addition, the temporal variations of the pressure at both sites are similar (more in section 4).

d. Turbulent flux calculation

Vertical turbulent momentum fluxes consist of coherent contributions from a range of eddy sizes. Assuming Taylor's hypothesis, increasing the time period for flux calculation would include flux contributions from large eddies and improve their sampling statistics. Because the size of the dominant turbulent eddies increases with height, the length of the data segment necessary to incorporate most of the turbulent flux using the eddy covariance method has to increase with height especially under near neutral and unstable conditions when large eddies contribute a significant portion of the turbulent flux. Steady turbulent fluxes can be precisely and objectively determined once the cumulative flux (i.e., fluxes integrated from small to large eddies) remains constant with increasing eddy size or decreasing frequency
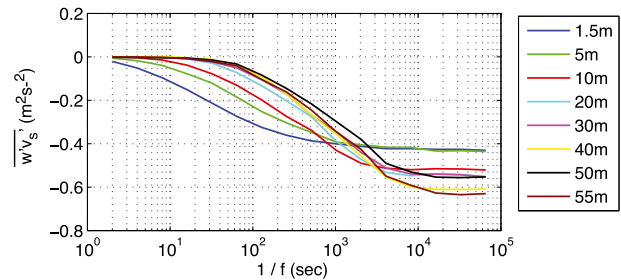

FIG. 3. An example of the cumulative momentum flux in the along-wind direction as a function of the integrated time scale using the Haar wavelet method. The data are from 1600 to 1700 UTC 15 Oct, when wind was relatively strong and the wind direction varied little with height.

(e.g., Fig. 3). Contribution from turbulence eddies with a time scale of $1/f$ in Fig. 3 to the cumulative flux is reflected in the change of the cumulative flux with $1/f$. The characteristics of the turbulent fluxes in Fig. 3 often occur when the atmosphere is near neutral—that is, for strong wind ($|z/L| > 100$, where L is the Obukhov length; Sun 2011).

Systematic underestimation of turbulent fluxes occurs when a sonic anemometer cannot respond fast enough to capture small eddies, or the pathlength of the sonic anemometer is too large to capture small turbulence eddies. As a result, the turbulent momentum flux close to the ground, where its dependence on the contribution of small eddies is significant, can be underestimated. Horst and Oncley (2006) investigated the underestimation using the transfer function as a function of eddy size relative to the pathlength for the sonic anemometer used during CASES-99 and found that the underestimation for the fluctuations of the individual wind components is significant for eddy sizes smaller than the pathlength. Applying their transfer functions to the covariance between the vertical and along-wind components, we find that the contribution of the eddies smaller than the pathlength to the cumulative momentum flux is less than 0.4% at our lowest sonic anemometer level of 0.5 m for moderate to strong winds. Thus, for a vertical flux difference of 10%, the flux difference error due to the pathlength averaging is less than 4% for the focus of this study, but may be significant for a very stably stratified flow.

Turbulent fluxes are uncertain when the environment is unsteady. The covariance spectra of turbulent fluxes can be influenced by sporadic and seemingly random (for lack of understanding) submeso motions, which increase uncertainty in turbulent flux estimates as demonstrated in Vickers and Mahrt (2003, 2006), Mahrt (2009, 2010), and Mahrt et al. (2012). This type of turbulent flux uncertainty is fundamentally different from instrument errors. To remove the influence of submeso motions on turbulent

flux estimates, we rely on visual inspection of the co-variance spectra. Overall, the impact of nonstationarity on turbulent fluxes is significant at all of the observation heights under weak winds. This nonstationarity is less important for moderate to strong winds, but visible occasionally.

The turbulent momentum flux in this study is calculated as cumulative multiresolution covariances using the Haar wavelet (Howell and Sun 1999) for every 30-min period, which is sufficient for the cumulative fluxes to achieve statistically stable estimates at all eight observation heights. The resulting cumulative fluxes from the Haar wavelet are similar to those using the Fourier method (Desjardins et al. 1989; Friehe et al. 1991). The cutoff time scale/frequency for determining the flux value from the cumulative cospectra is selected manually for each 30-min time segment to exclude the intermittent submeso flux from the turbulent flux.

To investigate relationships among the variations of all the terms in the momentum balance, all the observed and derived variables in this study are averaged for 30 min and include both daytime and nighttime data.

e. Coordinates

To ensure the quality of the measured pressure difference, we investigate its relation with other terms in the momentum balance in two coordinate systems. Since the wind observations are in Earth coordinates, which is a Cartesian coordinate system with the vertical direction opposite from gravity, and two horizontal directions— north–south (positive toward north) and east–west (positive toward east)—we calculate various terms in Earth coordinates first. However, there are advantages to analyzing the observations in natural coordinates (Holton 1979), which consist of along-wind, crosswind (positive direction is 90° counterclockwise from the wind direction), and vertical upward axes. The flow acceleration term only appears in the along-wind direction, and the relatively small Coriolis force with the Coriolis parameter f_c of approximately $O(10^{-4}\,\mathrm{s}^{-1})$ only appears in the crosswind direction. The turbulent momentum flux is much stronger in the along-wind direction than in the crosswind direction especially for strong winds. Analyzing observations in natural coordinates allows us to distinguish different momentum balances in the two perpendicular directions, which may have terms of very different magnitudes. To investigate vertical variations of turbulent fluxes in natural coordinates for moderate to strong winds, the 30-min-averaged wind vectors at all the observation levels are rotated to the wind direction at 5 m.

In prognostic studies, it is difficult to use natural coordinates because of varying wind direction. We use Earth coordinates to investigate airflow in response to different environmental conditions in section 3c. However, for diagnostic studies with known wind directions, we use natural coordinates.

3. Role of the horizontal pressure gradient in the momentum balance

We first investigate the characteristics of the horizontal pressure gradient $\nabla\overline{p}$ at 1.5 m above the ground. We find that the largest magnitude of $\nabla\overline{p}$ is from south; that is, the strongest horizontal pressure gradient occurs when high pressure is north of the site (Fig. 4a, red dots). However, strong winds at 5 m do occur for both southerly and northerly flow (Fig. 4a, black dots). The most intriguing result is in the directional difference between wind and $\nabla\overline{p}$ (Fig. 4b), where 50% of the observed wind is toward higher pressure; that is, the directional difference between $\nabla\overline{p}$ and wind is less than ±90° (the points between the two black lines in Fig. 4b). A significant fraction of these points is associated with large horizontal pressure gradients (red dots in Fig. 4b). A significant fraction of these points has strong wind as well. For these cases the wind direction is most accurate and varies little with height. Lack of observations of $\nabla\overline{p}$ between 180° and 360° in Fig. 4a is due to the observed small $\partial\overline{p}/\partial x$ compared to $\partial\overline{p}/\partial y$ and the predominantly negative $\partial\overline{p}/\partial x$ (Figs. 5a and 5b). Simulating the effect of uncertainty in the pressure measurement by arbitrarily adding a bias to $\partial\overline{p}/\partial x$ of $3 \times 10^{-5}\,\mathrm{hPa\,m}^{-1}$ or $\partial\overline{p}/\partial y$ of $3 \times 10^{-4}\,\mathrm{hPa\,m}^{-1}$ would result in some cases in this direction range. However, the shifting would not totally eliminate the WTHP phenomenon, especially for the strong wind and large pressure gradient cases.

The relationship between the directions of wind and $\nabla\overline{p}$ is further examined in terms of the fraction of the wind direction relative to the $\nabla\overline{p}$ direction in six wind speed categories (Figs. 4c and 4d). For wind speed stronger than $10\,\mathrm{m\,s}^{-1}$ (yellow vectors in Fig. 4d), all vectors are toward higher pressure despite the fact that the pressure gradient acts to decelerate the flow under these conditions. For wind speed less than $2\,\mathrm{m\,s}^{-1}$ (dark blue vectors in Fig. 4c), wind is observed in all directions relative to the $\nabla\overline{p}$ direction with slightly higher than 50% in the direction opposite to $\nabla\overline{p}$ (i.e., wind toward lower pressure).

We then examine the relationship between the magnitude of $\nabla\overline{p}$ and the wind speed at 5 m $\overline{S}$ in both Earth and natural coordinate systems (Figs. 5a–d). The 5-m level is the lowest observation level that had continuous turbulence measurements throughout the experiment. Along the y direction, which has the largest $\nabla\overline{p}$ and mean wind, $\partial\overline{p}/\partial y$ and the south wind component at 5-m $\overline{v}$ are
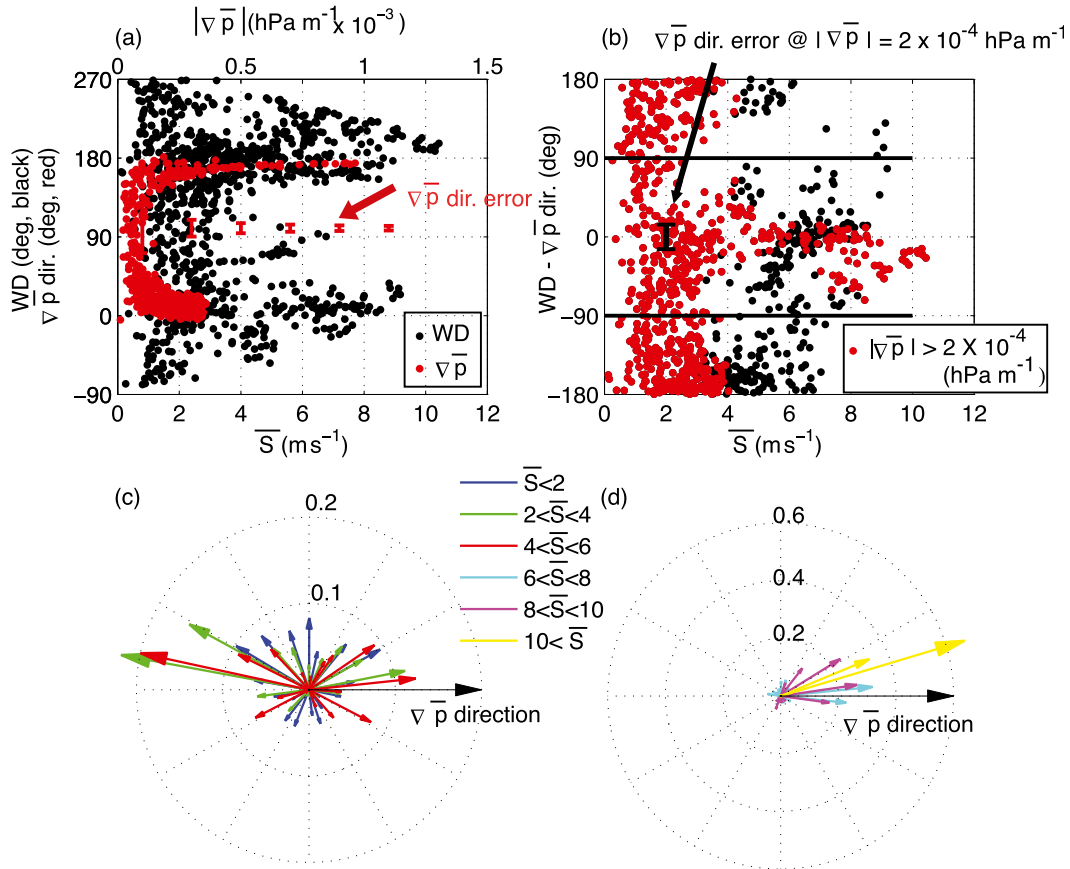
FIG. 4. (a) The relationships between the observed wind direction (WD) and wind speed at 5 m $\overline{S}$ (black), and between the direction of $\nabla\overline{p}$ and its magnitude $|\nabla\overline{p}|$ (red) for the entire 30-min-averaged dataset. The vertical red bars mark the directional error of $\nabla\overline{p}$ as a function of $|\nabla\overline{p}|$ due to inaccuracy of the pressure transducer. (b) The directional difference between WD and $\nabla\overline{p}$ as a function of $\overline{S}$, where the red dots denote $|\nabla\overline{p}| > 2 \times 10^{-4}$ hPa m^{-1}, the two horizontal black lines denote the directional boundaries for WTHP, and the black error bar marks the uncertainty of the $\nabla\overline{p}$ direction at $|\nabla\overline{p}| = 2 \times 10^{-4}$ hPa m^{-1}. (c),(d) The fractional distribution of WD relative to the $\nabla\overline{p}$ direction for six wind speed (m s^{-1}) categories. The length of each colored vector represents the fraction of the observations in that wind speed category. For example, all vectors of $\overline{S} > 10$ m s^{-1} (yellow) are toward higher pressure, and the sum of their lengths equals one. For the weak wind of $\overline{S} < 2$ m s^{-1}, the blue vectors are in all directions relative to the $\nabla\overline{p}$ direction, but the fraction in each direction is relatively small.

well correlated across the observed range of $\overline{v}$ (the green curve in Fig. 5a); furthermore, $\partial\overline{p}/\partial y$ and the north wind component are relatively well correlated as well (the magenta curve in Fig. 5a). In natural coordinates, the along-wind pressure gradient $\partial\overline{p}/\partial s$ and the crosswind pressure gradient $\partial\overline{p}/\partial n$ are well correlated with $\overline{S}$ (Figs. 5c and 5d) although the correlation differs for southerly and northerly winds (more discussion in section 3b). The large range of the $\partial\overline{p}/\partial y$ variation is reflected in $\partial\overline{p}/\partial s$ as the strong wind cases are dominated by a strong southerly wind component. The wind speed is never zero when $|\nabla\overline{p}|$ is small during CASES-99. WTHP (positive $\partial\overline{p}/\partial s$) occurs much more often under moderate to strong winds than WTLP (negative $\partial\overline{p}/\partial s$)—that is, 22% versus 6% for $\overline{S} > 5$ m s^{-1} (Figs. 5e and 5f).

To further investigate whether WTHP is realistic, we examine the relationships among various terms in the momentum balance. The momentum balance in Earth coordinates can be expressed as

$$\frac{d\overline{u}}{dt} - f_c\overline{v} = -\frac{1}{\overline{\rho}}\frac{\partial\overline{p}}{\partial x} - \frac{\partial\overline{w'u'}}{\partial z}, \qquad (5)$$

$$\frac{d\overline{v}}{dt} + f_c\overline{u} = -\frac{1}{\overline{\rho}}\frac{\partial\overline{p}}{\partial y} - \frac{\partial\overline{w'v'}}{\partial z}, \qquad (6)$$

where u, v, and w are wind components in x, y, and z directions; ρ is the air density; and the primes represent their perturbations relative to their 30-min means. The first and second terms on the left-hand side of both (5)
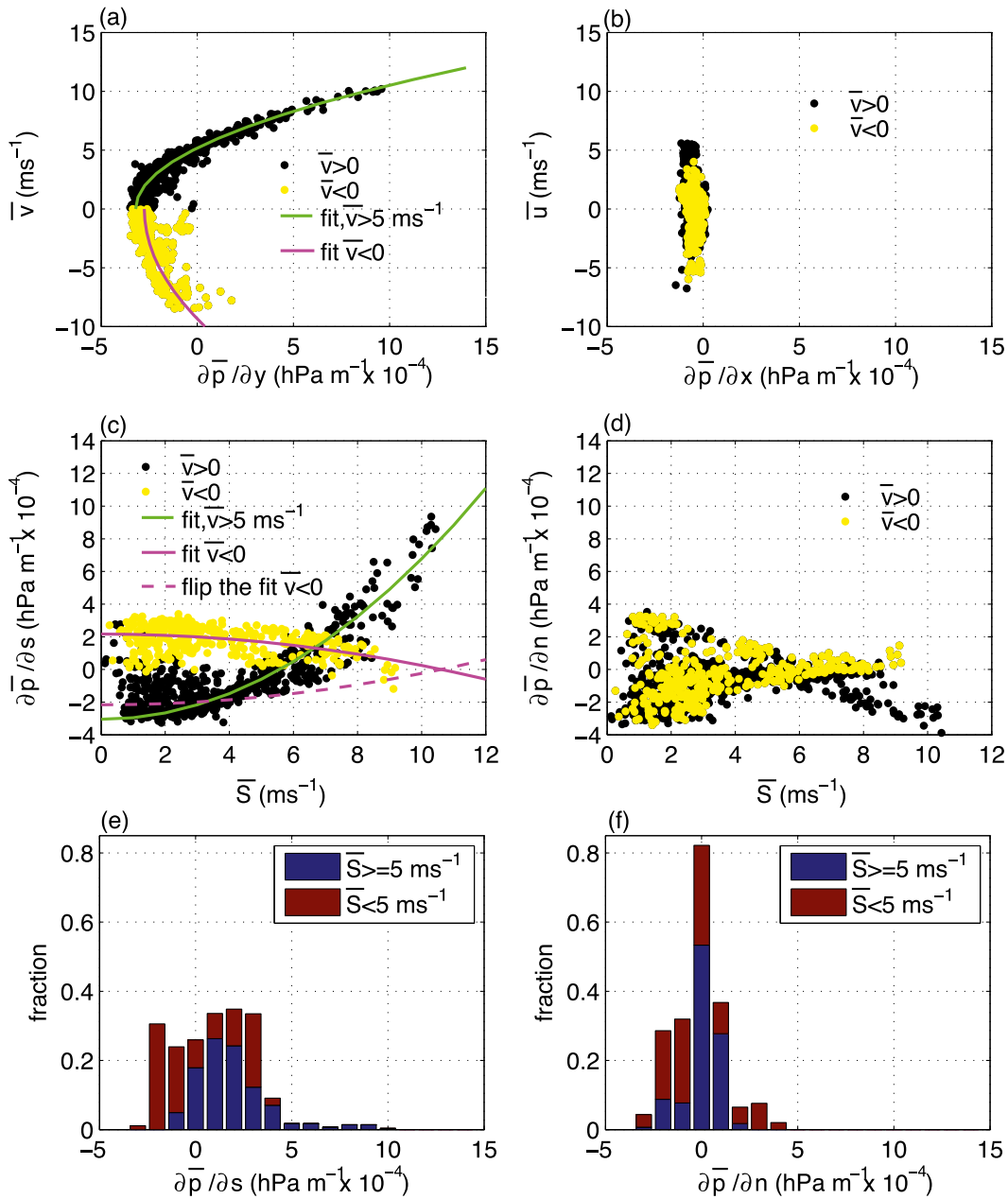
FIG. 5. The relationships (a) between $\partial\overline{p}/\partial y$ and $\overline{v}$ at 5 m, (b) between $\partial\overline{p}/\partial x$ and $\overline{u}$ at 5 m, (c) between $\partial\overline{p}/\partial s$ and $\overline{S}$ at 5 m, and (d) between $\partial\overline{p}/\partial n$ and $\overline{S}$. (e),(f) The fractional distributions of $\partial\overline{p}/\partial s$ and $\partial\overline{p}/\partial n$ in two wind speed categories, where positive $\partial\overline{p}/\partial s$ corresponds to WTHP. In (a)–(c), the black and yellow colors represent the cases for $\overline{v} > 0$ and for $\overline{v} < 0$, respectively. In (a), the green and magenta curves represent the fitted relationship between $\partial\overline{p}/\partial y$ and $\overline{v}^2$ for $\overline{v} > 5\,\mathrm{m\,s^{-1}}$ and for $\overline{v} < 0$, respectively. Similar to (a), the green and solid magenta curves in (c) represent the fitted relationship between $\partial\overline{p}/\partial s$ and $\overline{S}^2$ for $\overline{v} > 5\,\mathrm{m\,s^{-1}}$ and for $\overline{v} < 0$, respectively. The dashed magenta curve in (c) is the magenta curve flipped at $\partial\overline{p}/\partial s = 0$ for comparison with the green one.

and (6) are the flow acceleration and the Coriolis force, respectively, and the last term on the right-hand side of both equations is the vertical turbulent momentum transport. In the above momentum equations, the viscous stress associated with molecular motions is neglected (Garratt 1992). The horizontal momentum flux transport terms, such as $\partial\overline{u'u'}/\partial x$, $\partial\overline{u'v'}/\partial x$, $\partial\overline{v'v'}/\partial y$, and $\partial\overline{u'v'}/\partial y$, are assumed to be negligible, which should be valid at least under moderate to strong winds.

In comparison, the momentum balance in natural coordinates is expressed as (Schlichting and Gersten 2000)

$$\frac{d\overline{S}}{dt} = -\frac{1}{\rho}\frac{\partial \overline{p}}{\partial s} - \frac{\partial \overline{w'v'_s}}{\partial z}, \tag{7}$$

$$\frac{\overline{S}^2}{R} + f_c\overline{S} = -\frac{1}{\rho}\frac{\partial \overline{p}}{\partial n} - \frac{\partial \overline{w'v'_n}}{\partial z}, \tag{8}$$

where R is the curvature radius of the air parcel trajectory, and the subscripts s and n represent along- and crosswind components—that is, **s** and **n** (90° anticlockwise from **s**), respectively. Although the mean crosswind is zero in natural coordinates, the crosswind perturbation can contribute to the crosswind momentum flux. The concept of antitriptic and geotriptic balances mentioned in the introduction can be clearly identified in natural coordinates when the acceleration is zero. The momentum balance is antitriptic in the along-wind direction and geotriptic in the crosswind direction under equilibrium conditions. Overall, airflow cannot be in antitriptic balance unless the Coriolis force can be neglected in comparison with the curvature term in the crosswind direction; that is, a Rossby number, defined by $\mathrm{Ro} = f_c/(R\overline{S})$, is small.

The horizontal wind is traditionally thought to be forced by the horizontal pressure gradient while the contribution of the turbulent flux to the momentum balance is thought to be a drag, friction, internal friction, or frictional force in the literature (e.g., Jeffreys 1922; Johnson 1966). Because of zero wind speed at the ground, the turbulent momentum flux itself is downward near the ground (i.e., $\overline{w'v'_s} < 0$), and the turbulent momentum flux is commonly called turbulent stress. However the contribution of the turbulence transport to the momentum balance in (7) is not the turbulent momentum flux itself, but the vertical divergence of the turbulent momentum flux. If the magnitude of the turbulent stress decreases with height (i.e., $\partial \overline{w'v'_s}/\partial z > 0$), the influence of the turbulence on the momentum balance is a momentum sink in (7). In this situation, wind has to be toward lower pressure as shown in Fig. 6a. On the other hand, if the magnitude of the turbulent stress, or the negative turbulent momentum flux, increases with height (i.e., $\partial \overline{w'v'_s}/\partial z < 0$), the turbulence transport of the momentum contributes to the momentum balance as a momentum source in (7), then wind has to be toward higher pressure as shown in Fig. 6b.

Evidence of wind toward higher pressure has been reported in the literature. Prior to sonic anemometers, Sheppard et al. (1952) analyzed wind profiles collected from balloon measurements over the northeastern Atlantic for a 7-day period and concluded that in a baroclinic PBL, the surface wind is more likely to go toward higher pressure. Evidence for WTHP was also found for
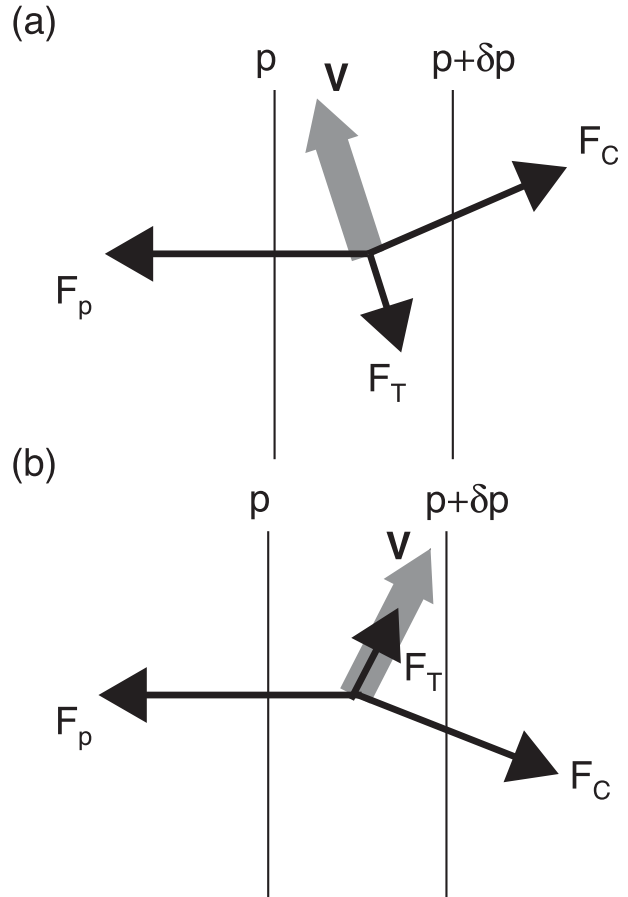

FIG. 6. Geotriptic balance among the horizontal pressure gradient force ($F_p = -\nabla\overline{p}$), the Coriolis force ($F_c = -f_c V\mathbf{n}$), and the turbulence transport of momentum ($F_T = -\partial \overline{w'v'_s}/\partial z\,\mathbf{s}$) for (a) $\partial \overline{w'v'_s}/\partial z > 0$ and (b) $\partial \overline{w'v'_s}/\partial z < 0$ if we assume $\partial \overline{w'v'_n}/\partial z$ is negligible. The vertical lines represent pressure contours.

mesolows—for example, by Adams-Selin and Johnson (2010), in which the Oklahoma Mesonet data of about 40–50-km spatial resolution were analyzed.

To better understand the WTHP phenomenon, especially under strong winds when the uncertainties of both the horizontal pressure gradient and turbulent momentum flux are relatively small, we conduct the following analyses:

1) We examine the relationship between the observed pressure gradient and the vertical variation of the turbulent momentum flux in natural coordinates to investigate whether the turbulent momentum transport can explain WTHP using the following two methods: First, we directly examine the vertical difference of the observed turbulent fluxes at the two levels around the $\nabla\overline{p}$ measurement level. Second, we apply the bulk formula to relate the observed turbulent momentum flux with wind speed at the two levels and analyze the
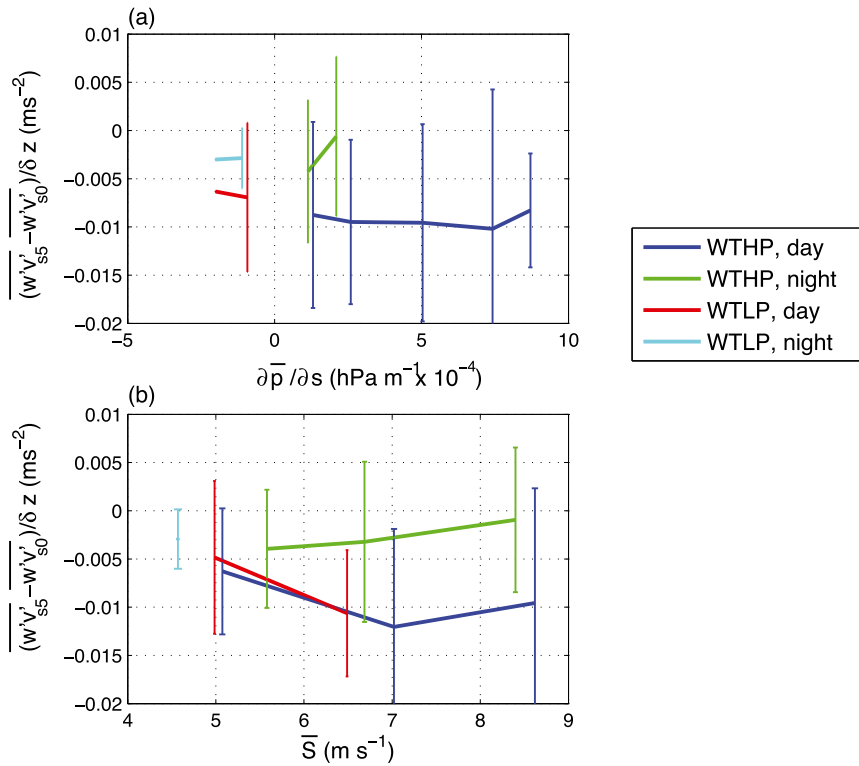
FIG. 7. The estimated vertical derivative of the along-wind turbulent momentum fluxes between 5 m (represented by subscript 5) and the lowest sonic-anemometer level (represented by subscript 0) as a function of (a) $\partial \overline{p}/\partial s$ and (b) $\overline{S}$ at 5 m for four categories. "Night" and "day" represent the data from local nighttime and daytime. The vertical lines represent the standard deviation of the derivatives in each average bin. Positive $\partial \overline{p}/\partial s$ corresponds to WTHP. All the data used here are for $\overline{S} > 5\,\mathrm{m\,s^{-1}}$.

vertical difference from the fitted relationship between turbulent momentum fluxes and mean wind speeds. The second method depends on the averaged relationship between turbulence and wind speed but avoids the flux uncertainty in each flux estimate.

2) We then investigate the reason behind the observed relationship between $\partial \overline{p}/\partial s$ and $\overline{S}$ in Fig. 5c and between $\partial \overline{p}/\partial y$ and $\overline{v}$ in Fig. 5a based on the fitted dependence of the turbulent momentum flux on wind speed under moderate to strong winds.

3) We then explore the possibility of WTHP by using a simple PBL mixing model. The exercise here is to demonstrate that WTHP can happen at least under specified realistic baroclinic conditions and not to explore sufficient and necessary conditions for WTHP.

a. Relationship between the horizontal pressure gradient and the observed turbulent momentum flux

To investigate the vertical variation of the momentum flux at the pressure-sensor level, we use the turbulence measurements at 5 m and at the lowest sonic-anemometer level (0.5 or 1.5 m) (Fig. 7). We focus on the turbulent momentum flux for $\overline{S} > 5\,\mathrm{m\,s^{-1}}$ as the flux uncertainty generally increases with decreasing wind speed owing to unknown sporadic submeso motions. In addition, strong turbulent mixing associated with strong wind reduces vertical variations of wind direction to the point that the directional variation of the turbulent flux is negligible. However even under strong winds, the submeso fluxes can occasionally influence the turbulent flux at higher levels (section 2), which is reflected in the relatively large standard deviation of the vertical momentum flux difference for a relatively small range of wind speed in Fig. 7b. Under moderate to strong winds, the covariance spectra at the observation heights are similar to the ones in Fig. 3; that is, the contribution of large eddies increases with height while the contribution of small eddies decreases with height. We average the vertical flux difference in four categories depending on whether wind is toward higher or lower pressure and day or night. Overall, the magnitude of the downward turbulent momentum flux is larger at the upper level than the lower level in all the categories and the vertical flux difference may be

slightly larger during daytime than at night perhaps because of the diurnal variation of the atmospheric stability. On average, the vertical flux difference is larger for WTHP ($\partial \overline{p}/\partial s > 0$) than for WTLP ($\partial \overline{p}/\partial s < 0$) because both the wind speed and the horizontal pressure gradient are stronger for WTHP than for WTLP during CASES-99 (Fig. 7a).

Traditionally, the turbulent flux is assumed constant with height in the surface layer. If the increased contribution of large eddies to the turbulent flux with height exactly compensates for the decreased contribution of small eddies, the turbulent flux would be constant with height. The results in Fig. 7 imply that the increase of the large-eddy contribution to the turbulent flux is greater than the decrease of the small-eddy contribution under moderate to strong winds, which is also evident in Fig. 3. Therefore, the observation of the vertical variation of the turbulent momentum flux suggests the existence of WTHP as long as the airflow is approximately in equilibrium, which is independent of the pressure measurement.

Sun et al. (2012) found that when the wind is below a threshold wind value for a given observation height in a stably stratified atmosphere, turbulence generated at the ground rapidly decreases with height. However, once wind speed is stronger than the threshold at the observation height, large turbulent eddies, which scale with the layer depth, can be generated by the bulk shear—that is, a strong shear across the entire layer between the observation height and the ground. Similar results were found by Mahrt et al. (2012) and Van de Wiel et al. (2012). As shown in Fig. 3, the large eddies can effectively contribute to the turbulent flux through their large amplitudes. As the amplitude of large eddies decreases toward the ground, the contribution of the large eddies to the turbulent momentum flux decreases significantly.

Turbulence can also be generated by strong local instabilities (either thermal or shear instability) well above the ground; for example, below a nocturnal low-level jet (LLJ) (Banta et al. 2002), turbulence can increase with height (i.e., the so-called upside-down nocturnal boundary layer). Under this situation, the downward turbulent momentum flux can converge vertically (Banta et al. 2006), corresponding to a momentum source. Therefore, the magnitude of the downward turbulent momentum flux can increase with height not only under a nocturnal LLJ, but also with strong winds when the contribution of large eddies to the turbulent flux is enhanced. As a result of the increase in magnitude of the turbulent momentum flux with height, the vertical turbulent momentum flux converges toward the surface and provides a momentum source, which can approximately balance the strong wind toward higher pressure.

An increase of the turbulent momentum flux with height has also been observed by Pennell and LeMone (1974) and Desjardins et al. (1989) using aircraft data. The possible occurrence of WTHP and the vertical increase of the turbulent momentum flux are further investigated later in this section by using a simple PBL balance model.

For the crosswind momentum balance, the relevance of the curvature term in the crosswind momentum balance compared to the Coriolis force is determined by the Rossby number defined at the beginning of this section. For a $10 \, \text{m s}^{-1}$ wind, the curvature term is negligible for $R > 10 \, \text{km}$. The observed nearly linear relationship between $\partial \overline{p}/\partial n$ and $\overline{S}$ for $\overline{S} > 5 \, \text{m s}^{-1}$ for both southerly and northerly winds in Fig. 5d suggests that the curvature term, $\overline{S}^2/R$, is relatively small. For wind speed stronger than about $5 \, \text{m s}^{-1}$, a significant fraction of the large values of $\partial \overline{p}/\partial n$ are negative (Fig. 5d). Negative $\partial \overline{p}/\partial n$ is opposite to the Coriolis force in (8). This result implies that the Coriolis force is relatively important in the crosswind momentum balance at the CASES-99 site. The crosswind momentum flux is much smaller than the along-wind flux, and its vertical variation is not systematic as for the along wind; therefore, we do not examine it here.

b. Relationship between wind speed and the along-wind horizontal pressure gradient

We investigate the relationship between $\partial \overline{p}/\partial s$ and $\overline{S}$ in Fig. 5c, which is also similar to the relationship between $\partial \overline{p}/\partial y$ and $\overline{v}$ in Fig. 5a. Assuming the along-wind pressure gradient balances the vertical convergence of the along-wind turbulent momentum flux, we can associate the horizontal pressure gradient with the vertical difference of the turbulent momentum flux expressed in the surface bulk formula. Applying the surface bulk formula for the along-wind momentum flux at both 5 m (represented by subscript 5) and the lowest sonic anemometer level (0.5 or 1.5 m, represented by subscript 0), the along-wind momentum flux can be expressed as

$$\overline{w'v_s'}|_5 = -C_D \overline{S}^2 \quad \text{and} \tag{9}$$

$$\overline{w'v_s'}|_0 = -C_{D0} \overline{S}_0^2, \tag{10}$$

where

$$C_{D0} = C_D - \delta C_D, \tag{11}$$

$$\overline{S}_0 = \overline{S} - \delta S, \tag{12}$$

C_D is the drag coefficient at 5 m, and δC_D and $\delta \overline{S}$ are the departures of C_D and $\overline{S}$ at the lowest sonic anemometer level from their 5-m values, respectively. Substituting

(9)–(12) into (7) and assuming the atmosphere is in equilibrium, we have antitriptic balance,

$$\frac{1}{\overline{\rho}}\frac{\partial \overline{p}}{\partial s} \simeq -\frac{\overline{w'v'_s}|_5 - \overline{w'v'_s}|_0}{\delta z}$$

$$= \frac{1}{\delta z}[C_D \overline{S}^2 - (C_D - \delta C_D)(\overline{S} - \delta S)^2]$$

$$= \frac{C_D \overline{S}^2}{\delta z}\left[1 - \left(1 - \frac{\delta C_D}{C_D}\right)\left(1 - \frac{\delta S}{\overline{S}}\right)^2\right] = \frac{C_D \overline{S}^2}{\delta z}A,$$

(13)

where

$$A \equiv 1 - \left(1 - \frac{\delta C_D}{C_D}\right)\left(1 - \frac{\delta S}{\overline{S}}\right)^2, \qquad (14)$$

and δz is the vertical distance between 5 m and the lowest sonic anemometer level. If both A and C_D are invariant at a fixed z, the antitriptic balance along the wind direction in (13) implies

$$\frac{\partial \overline{p}}{\partial s} \sim \overline{S}^2. \qquad (15)$$

In addition, if $A > 0$, (13) also implies that the magnitude of negative $\overline{w'v'_s}$ increases with height.

We examine A in (14) using the observations at 0.5, 1.5, and 5 m for $\overline{S} > 5 \text{ m s}^{-1}$. Because $\delta\overline{S}/\overline{S}$ approaches a constant as $\overline{S}$ increases no matter whether $\overline{S}_0$ is at 1.5 or 0.5 m (Fig. 8b), and C_D is approximately invariant under neutral conditions (strong winds) at a given z (Fig. 8a), A is invariant under strong winds. We relate the observed $\partial\overline{p}/\partial s$ and $\overline{S}$ for $\overline{v} > 5 \text{ m s}^{-1}$ and for $\overline{v} < 0$ using the following relationship:

$$\frac{\partial \overline{p}}{\partial s} = a\overline{S}^2 + b, \qquad (16)$$

where a (hPa s^2 m^{-3}) and b (hPa m^{-1}) are fitted constants. The coefficient b allows for a small adjustment because overall, the observed flow seems not exactly in equilibrium. Figure 5c shows that the observed $\partial\overline{p}/\partial s$ is indeed closely related to the wind speed squared for $\overline{v} > 5 \text{ m s}^{-1}$ and for $\overline{v} < 0$, which suggests that antitriptic balance is approximately valid in the along-wind direction at least for the moderate to strong winds associated with the WTHP events. The relatively large systematic deviation of the observed low winds from the fitted relationship for $\overline{v} > 5 \text{ m s}^{-1}$ (green line in Fig. 5c) suggests that the atmospheric stability, which we ignore in the derivation of (15), could be a factor in the relationship between $\partial\overline{p}/\partial s$ and $\overline{S}$. Since the data for $\overline{v} < 0$ in Fig. 5c are dominated by relatively weak winds, the observed
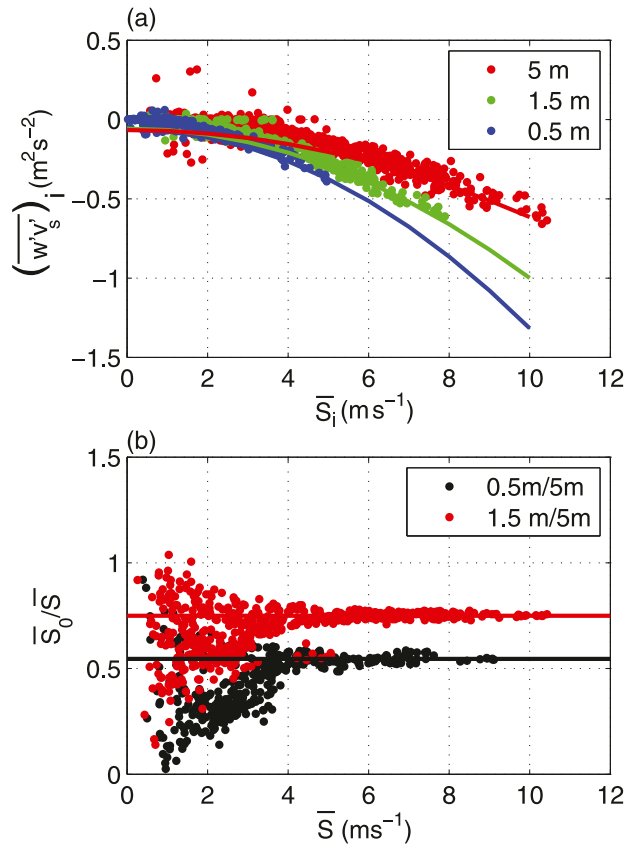

FIG. 8. (a) The along-wind momentum flux $(\overline{w'v'_s})_i$ as a function of wind speed $\overline{S}_i$ at $i = 0.5$, 1.5, and 5 m above the ground. The curves are least-square fits of $(\overline{w'v'_s})_i$ as functions of $\overline{S}_i^2$ at the three levels using only observations when wind speed at 5 m $\overline{S} > 5 \text{ m s}^{-1}$. (b) The wind speed ratios between 5-m $\overline{S}$ and the lowest sonic anemometer level $\overline{S}_0$ as functions of $\overline{S}$. The horizontal lines in (b) mark the constant ratios at the strong wind limit at the two levels.

different relationships between $\partial\overline{p}/\partial s$ and $\overline{S}$ for $\overline{v} > 5 \text{ m s}^{-1}$ and $\overline{v} < 0$ may also reflect the influence of atmospheric stability on the relationship. In addition, antitriptic balance may not be valid under weak winds because nonstationarity under the influence of sporadic submeso motions can be an issue, and all the momentum terms may have similar magnitudes. Similarly $\partial\overline{p}/\partial y$ is well correlated to $\overline{v}^2$ as shown in Fig. 5a.

Using the fitted relationship between the observed $\overline{w'v'_s}$ and $\overline{S}$ at 0.5, 1.5, and 5 m for $\overline{S} > 5 \text{ m s}^{-1}$ (Fig. 8a), we obtain C_D at each level. Using both the estimated C_D and $\delta\overline{S}/\overline{S}$ at each level, we find positive A no matter whether the lowest sonic anemometer was at 0.5 or 1.5 m. Positive A suggests that on average the magnitude of the downward turbulent momentum flux increases with height; that is, the turbulent momentum flux transfer is a source term in the momentum balance, which allows WTHP. Therefore, the observed relationship between the quadratic wind

speed and the horizontal pressure gradient further suggests the existence of WTHP.

c. A simple mixing model in barotropic and baroclinic environments

To theoretically explore the possibility of the surface wind blowing toward higher pressure and the magnitude of the downward momentum flux increasing with height, we present here an analysis using a simple PBL eddy diffusivity model for both barotropic and baroclinic conditions in geotriptic balance. To be able to specify the vertical variation of the horizontal pressure gradient through the geostrophic relationship, we use Earth coordinates. Using the geostrophic relationship,

$$f_c U_g = -\frac{\partial \overline{p}}{\partial y} \quad \text{and} \tag{17}$$

$$f_c V_g = \frac{\partial \overline{p}}{\partial x}, \tag{18}$$

the geotriptic equations of motion can be written as

$$-f_c[\overline{v}(z) - V_g(z)] = \frac{\partial}{\partial z}\left[K_m(z)\frac{\partial \overline{u}}{\partial z}\right] \quad \text{and} \tag{19}$$

$$f_c[\overline{u}(z) - U_g(z)] = \frac{\partial}{\partial z}\left[K_m(z)\frac{\partial \overline{v}}{\partial z}\right], \tag{20}$$

where U_g and V_g are geostrophic wind components in x and y directions, and $K_m(z)$ is the eddy viscosity. In (19) and (20), the momentum fluxes in x and y directions are

$$\frac{\tau_x(z)}{\overline{\rho}} = -K_m(z)\frac{\partial \overline{u}}{\partial z} \quad \text{and} \tag{21}$$

$$\frac{\tau_y(z)}{\overline{\rho}} = -K_m(z)\frac{\partial \overline{v}}{\partial z}. \tag{22}$$

We neglect any dependence of the eddy viscosity on baroclinity (Arya and Wyngaard 1975), and base our $K_m(z)$ on the expression given by Collins et al. (2004) for neutral conditions,

$$K_m(z) = u_{*0}\kappa z\left(1 - \frac{z}{h}\right)^2, \tag{23}$$

where h is the PBL height, κ is the von Kármán constant, and u_{*0} is the surface friction velocity. We slightly modify $K_m(z)$ by an exponential function so that it transits smoothly into the free troposphere at $z = h$ and results in a well-behaved analytical solution for (19) and (20). Writing it in a dimensionless form, we have

$$\tilde{K}_m(\zeta) = \frac{K_m(z)}{u_{*0}h} \tag{24}$$

$$= \kappa\zeta(1 - 0.9\zeta)^2 \exp(-\zeta^6) + \tilde{K}_{m0}, \tag{25}$$

where $\zeta = z/h$ and $\tilde{K}_{m0} = 0.0002$, which is plotted in Fig. 9a.

We assume a baroclinic environment where both U_g and V_g increase linearly with height from $U_g = -10\,\text{m s}^{-1}$ and $V_g = -1\,\text{m s}^{-1}$ at $\zeta = 0$ to $\partial U_g/\partial z = \partial V_g/\partial z = 0$ for $\zeta > 1$. We consider two cases for $0 < \zeta \leq 1$: case 1, $\partial U_g/\partial z = \partial V_g/\partial z = 0.02\,\text{s}^{-1}$, and case 2, $\partial U_g/\partial z = \partial V_g/\partial z = -0.005\,\text{s}^{-1}$. The vertical variation of geostrophic wind in cases 1 and 2 corresponds to equal temperature gradients in x and y direction of about 6×10^{-5} and $-1.5 \times 10^{-5}\,\text{K m}^{-1}$, respectively. For comparison, we also present a barotropic case with the same $\tilde{K}_m(z)$, $U_g = 10\,\text{m s}^{-1}$, and $V_g = 19\,\text{m s}^{-1}$, which are the geostrophic wind values at $z = h$ for case 1. In addition, we choose $u_{*0} = 0.5\,\text{m s}^{-1}$ and $h = 10^3\,\text{m}$ for all the cases. The above cases are chosen only to demonstrate different baroclinic situations and a barotropic situation, not to simulate any observed cases as we do not know the vertical variation of the horizontal pressure gradient nor the geostrophic wind during CASES-99.

The resulting wind for the barotropic case is toward lower pressure and the magnitude of the downward momentum flux decreases with height (Figs. 9b,c,e). For case 1, which represents warm advection (see below), the surface wind is toward higher pressure, and the magnitude of the downward momentum flux increases with height up to $z \simeq 360\,\text{m}$ and decreases above it (Figs. 9b–e). Similar to the barotropic case, the surface wind in case 2, which represents cold advection (see below), is toward lower pressure and the magnitude of the downward momentum flux decreases with height throughout the PBL (Figs. 9b,c,e,f).

Hoxit (1974) investigated the different baroclinic effects of cold and warm advection on ageostrophic winds by extending the work of Sheppard et al. (1952). He found that baroclinity increases (decreases) the ageostrophic wind components toward lower pressure in cold (warm)-air advection. Arya and Wyngaard (1975) also found that the surface cross-isobar angle is a function of the thermal wind, with larger values occurring for warm-air advection and smaller values for cold-air advection.

In case 1, the thermal wind is southwesterly; that is, the air is generally warmer in the southeast sector and colder in the northwest sector (Fig. 10a). The thermal wind results in the geostrophic wind turning clockwise.
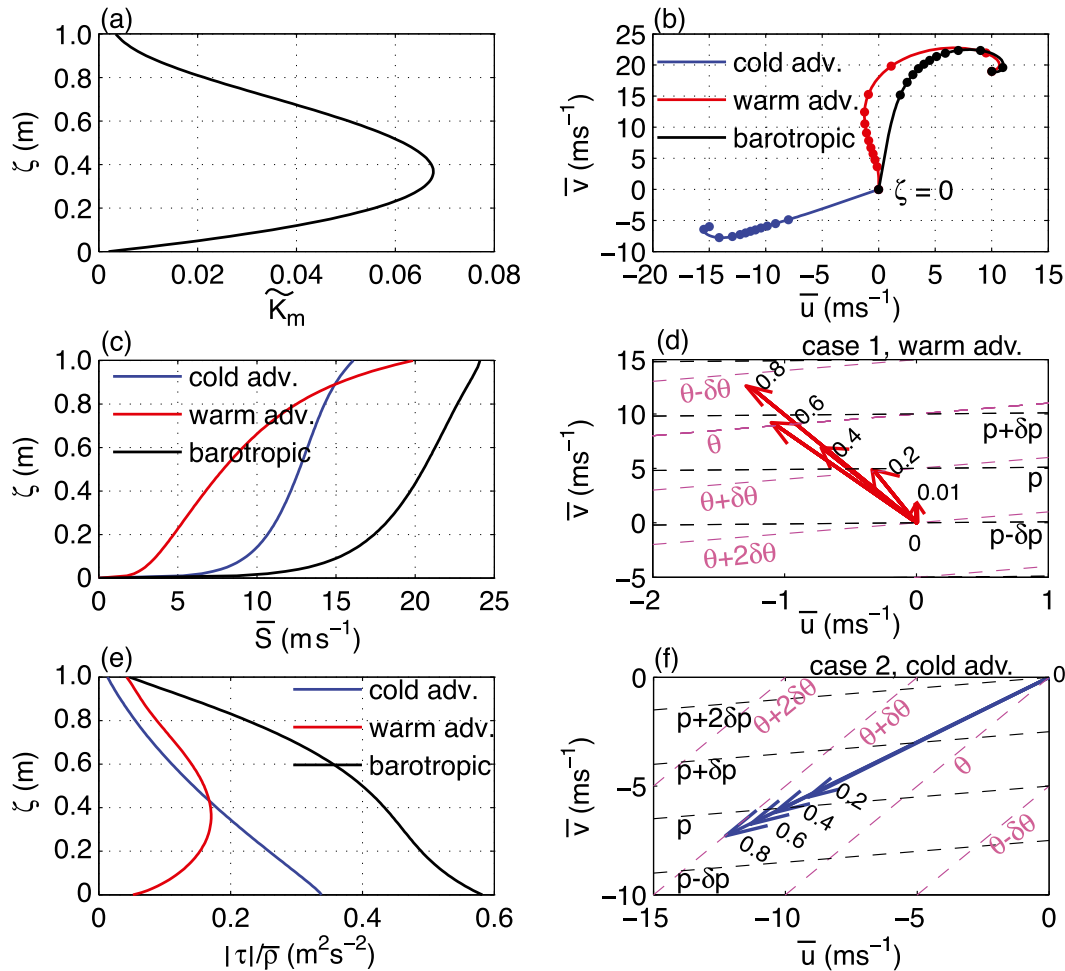
FIG. 9. (a) The normalized eddy viscosity as a function of the normalized height ($\zeta = z/h$), (b) the hodograph in Earth coordinates, and (c) the wind speed $\overline{S}$ and (e) the turbulent momentum flux as a function of ζ for the three cases. (d),(f) The wind vectors at several values of ζ, horizontal pressure contours (black dashed lines), and temperature contours (magenta dashed lines) for cases 1 and 2 are shown.

As the surface southerly wind approaches the geostrophic wind with height, the resulting south wind in this case blows from the warm to the cold sector throughout the PBL and toward higher pressure. These results suggest that warm-air advection can lead to WTHP.

In contrast, the thermal wind is northeasterly for case 2, and the air is warmer in the northwest sector and colder in the southeast sector (Fig. 10b). Thus, the thermal wind leads to the geostrophic wind turning counterclockwise. The resulting east-northeast flow in this case blows from the cold to the warm sector throughout the PBL, and the wind is toward lower pressure.

These three cases show examples of the equilibrium momentum balance when wind is toward higher/lower pressure. It remains to be determined whether warm advection is a necessary condition for WHTP or whether the dynamic characteristics of strong winds can also produce WTHP. A more thorough analysis is required to demonstrate the necessary and sufficient conditions for wind toward higher/lower pressure.

4. Discussion

a. Duration of wind toward higher pressure

As the CASES-99 observation domain is about $500\,\mathrm{m} \times 500\,\mathrm{m}$, we can only address the duration of the WTHP occurrence and not the spatial scale. As expected, the number of WTHP events decreases with the event duration (Fig. 11), where a WTHP event is defined as a continuous time period when the directional difference between wind and $\nabla\overline{p}$ remains less than a specified value. In Fig. 11, we choose two values, $\pm45°$ and $\pm90°$, to evaluate the sensitivity of the number frequency of the
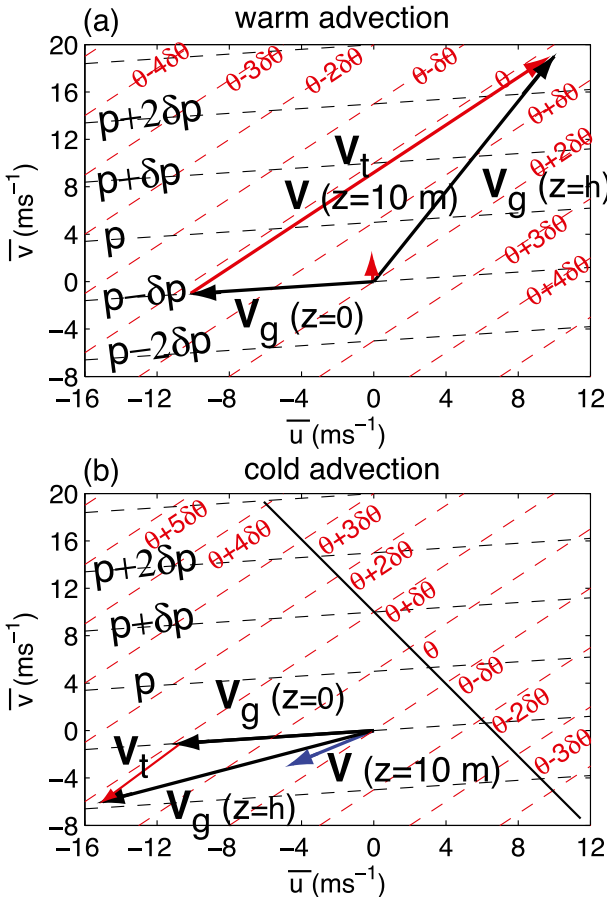
FIG. 10. The specified geostrophic wind $\mathbf{V}_g$ at $z = 0$ and h, the corresponding thermal wind $\mathbf{V}_t$ within the PBL, and the wind vector $\mathbf{V}$ at $z = 10\,\mathrm{m}$ for (a) the warm advection (red vector) and (b) the cold advection (blue vector), respectively. The black and red dashed lines are the pressure and temperature contours, respectively.
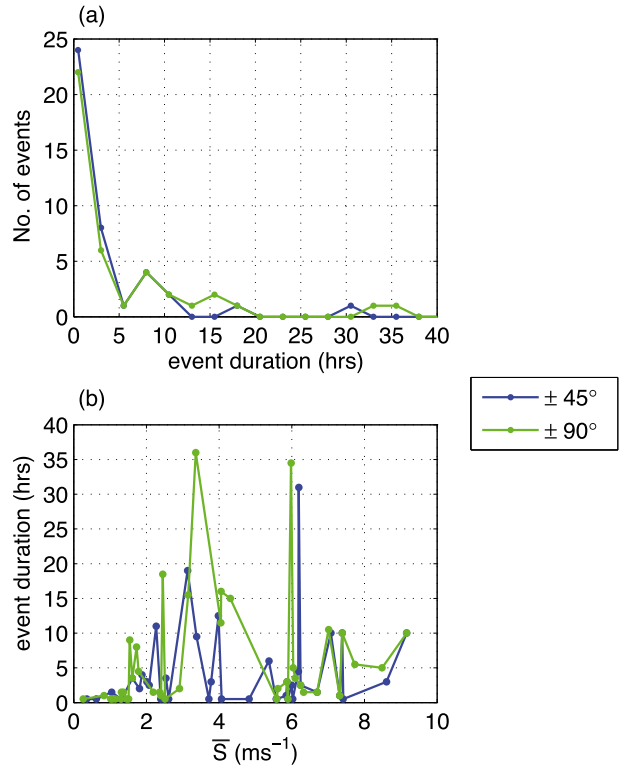

FIG. 11. (a) The number of WTHP events as a function of the event duration, and (b) the correlation between the event duration and the mean wind speed of the event at 5 m for the two definitions of WTHP.

WTHP event to the event definition. There are a number of events that last longer than 10 h no matter which definition we use. By relating the averaged wind speed during each event and the length of each event, we find that the longest WTHP event lasted about 30 h and occurred at a relatively strong wind of $6\,\mathrm{m\,s^{-1}}$ for the $\pm45°$ definition (Fig. 11b). If we relax the definition to $\pm90°$, another WTHP event longer than 30 h occurred at about $3\,\mathrm{m\,s^{-1}}$. These results suggest that the WTHP event is not just a random, small-scale phenomenon; it may occur on the synoptic scale as well.

The strongest WTHP event, occurring on 15 October, is associated with a strong low pressure system. On this day, the synoptic map indicates that Hurricane Irene was southeast of Florida, and a low-pressure center moved slowly southeastward toward the CASES-99 site. The surface pressure gradient between the low pressure northwest of the site and the low pressure associated with

Irene, which were separated by a high-pressure ridge, was large. Shortly after 1500 UTC (1000 LDT), the surface pressure started to decrease and the strength of the southerlies started to increase in the Kansas area. The surface pressure remained relatively low and steady for about 5 h after the large initial decrease. The horizontal pressure gradient based on two Automated Surface Observing System (ASOS) stations (Nadolski 1998) separated by about 20 km southwest of the CASES-99 site was on the same order of magnitude as the one observed at the CASES-99 site. In addition, the National Weather Service (NWS) reported a maximum wind gust of about $15\,\mathrm{m\,s^{-1}}$ around 2200 UTC over the surrounding central Kansas area of approximately $200\,\mathrm{km} \times 200\,\mathrm{km}$, which was consistent with the strong wind associated with the strong horizontal pressure gradient observed at the CASES-99 site. Therefore, the strongest WTHP observed at the site may be similar to the physical process in the mesolows described in Johnson (2001) although no severe precipitation was involved.

Because the magnitude of the turbulent flux has to decrease toward the PBL top, the observed increase in magnitude of the downward along-wind turbulent flux

with height for WTHP has to reverse and decrease with height somewhere higher up within the PBL as demonstrated in the simple PBL balance model in section 3c. This suggests that the PBL during CASES-99 had to be baroclinic if the PBL was in quasi equilibrium. Thus, the increasing contribution of large eddies to the turbulent flux observed during CASES-99 could be associated with baroclinity. However, whether the baroclinity is the key behind WTHP needs to be further explored.

b. Wind toward lower pressure and the weak southerly wind

For the observed WTLP cases during CASES-99, both the wind speed and the horizontal pressure gradient are mostly weak. The weak southerly wind is found to be dominated by the nighttime cold air moving northward from the small gullies south and southwest of the 60-m tower. When this happens, the temperature at tower 5 tends to be about 0.5°C or more lower than that at tower 2, and the pressure is about 0.02 hPa higher at tower 5 than at tower 2. Interestingly, the weak southerly wind at night is dominated by WTLP events, which is consistent with the cold advection case from the simple PBL balance model in section 3c.

During CASES-99, all the WTLP cases have weak winds except for a few moderate wind cases. The magnitude of the downward along-wind momentum flux increases with height for those cases, similar to WTHP with the same wind conditions. For those cases, the flow acceleration cannot be neglected in the momentum balance as both the horizontal pressure gradient and the vertical turbulent transport are momentum sources. Our observation of few strong wind cases with WTLP is another indication of lack of significant flow acceleration during CASES-99. Further investigation is needed.

c. Antitriptic and geotriptic balances

The observations in this study demonstrate that the vertical turbulent momentum transfer, which appears in both antitriptic and geotriptic balances, needs to be interpreted correctly. It is not sufficient to know just the surface momentum flux when considering the momentum balance. The vertical momentum transfer by the turbulent flux does not always act as a drag or "friction" as it is often called; it can be a momentum source in a baroclinic environment. Consequently, the surface wind may be driven by not only the horizontal pressure gradient but also by the vertical convergence of the turbulent momentum flux.

The importance of the Coriolis force in the momentum balance relative to flow acceleration can be easily evaluated in natural coordinates because it only appears in the crosswind direction. Based on the observed approximately linear relationship between the 30-min-averaged crosswind pressure gradient and wind speed for either $\bar{v} > 0$ or $\bar{v} < 0$, R must be relatively large during CASES-99. Thus, the observations suggest that $\mathrm{Ro} = \bar{S}/(f_c R)$ is relatively small and the Coriolis force is important in the crosswind direction during CASES-99. Therefore, the airflow during CASES-99 is approximately geotriptic.

5. Summary

Our unique dataset is of sufficient quality to take a new look at the momentum balance at the bottom of the atmosphere. We find that about 50% of the time during CASES-99, wind is toward higher pressure, which includes all of the observed winds. If we restrict the observations to wind speed at 5 m above the ground stronger than $5\,\mathrm{m\,s}^{-1}$, wind toward higher pressure occurred in about 40% of these cases, or about 20% of the entire time. For these moderate to strong wind cases, the horizontal pressure gradient is large, the turbulent flux uncertainty is relatively small, and the vertical variation of wind direction is negligible. As demonstrated in Sun et al. (2012), the bulk shear in strong wind cases can generate large eddies. We find that the contribution of large eddies to the turbulent momentum flux increases with height. Through the vertical turbulent momentum flux transport, this provides a mechanism for a momentum source above the ground instead of a sink or an "internal friction" as sometimes described. Because of this momentum source, the surface wind can be toward higher pressure, which acts to decelerate the airflow (Fig. 6b). Based on the relationship between turbulence and mean wind speed under antitriptic balance in the along-wind direction, the observed approximate relationship between the along-wind pressure gradient and the quadratic wind speed under strong winds further suggests an approximate balance between the horizontal pressure gradient and the vertical turbulent momentum transfer. The observed wind toward lower pressure occurs most often with weak southerly wind, which is often associated with cold advection from the gullies south and southwest of the site. Thus, wind toward higher pressure is not only observed directly through wind and pressure measurements, but it is also indirectly confirmed through the observed vertical convergence of the turbulent momentum flux and the relationship between wind speed and horizontal pressure gradient.

The observed crosswind pressure gradient is approximately linearly related to the wind speed especially under strong wind, suggesting that the curvature term and the Rossby number associated with the radius of the air trajectory are small. The observed negative pressure

gradient in the crosswind direction further implies the contribution of the Coriolis force in the crosswind momentum balance. Thus airflow during CASES-99 is approximately geotriptic.

Using a simple PBL eddy diffusivity model, we find that warm advection can lead to the magnitude of the downward turbulent momentum flux increasing with height and wind blowing toward higher pressure, while cold advection or a barotropic PBL results in the magnitude of the turbulent momentum flux decreasing with height and wind blowing toward decreasing pressure. The role of the baroclinity for WTHP from the model result is consistent with our observations of WTLP being dominated by cold advection and ageostrophic wind studies in the literature. However, the connection between the increasing contribution of large eddies to the turbulent flux and the baroclinity as well as the necessary and sufficient conditions for wind toward higher/lower pressure remains to be further investigated.

REFERENCES

Adams-Selin, R. D., and R. H. Johnson, 2010: Mesoscale surface pressure and temperature features associated with bow echoes. *Mon. Wea. Rev.,* **138,** 212–227.

Akyüz, F. A., H. Liu, and T. Horst, 1991: Wind tunnel evaluation of PAM II pressure ports. *J. Atmos. Oceanic Technol.,* **8,** 323–330.

Arya, S. P. S., and J. C. Wyngaard, 1975: Effect of baroclinicity on wind profiles and the geostrophic drag law for the convective planetary boundary layer. *J. Atmos. Sci.,* **32,** 767–778.

Banta, R. M., R. K. Newsom, J. K. Lundquist, Y. L. Pichugina, R. L. Coulter, and L. Mahrt, 2002: Nocturnal low-level jet characteristics over Kansas during CASES-99. *Bound.-Layer Meteor.,* **105,** 221–252.

——, Y. L. Pichugina, and W. A. Brewer, 2006: Turbulent velocity-variance profiles in the stably boundary layer generated by a nocturnal low-level jet. *J. Atmos. Sci.,* **63,** 2700–2719.

Bell, G. D., and L. F. Bosart, 1988: Appalachian cold-air damming. *Mon. Wea. Rev.,* **116,** 137–161.

Bernhardt, K., 1983: Integral approach to the antitriptic flow. *Z. Meteor.,* **33,** 322–328.

Colle, B. A., and C. F. Mass, 1996: An observational and modeling study of the interaction of low-level southwesterly flow with the Olympic Mountains during COAST IOP 4. *Mon. Wea. Rev.,* **124,** 2152–2175.

Collins, W. D., and Coauthors, 2004: Description of the NCAR Community Atmosphere Model (CAM 3.0). NCAR Tech. Rep. NCAR/TN-464+STR, 214 pp.

Cuxart, J., G. Morales, E. Terradellas, and C. Yagüe, 2002: Study of coherent structures and estimation of the pressure transport terms for the nocturnal stable boundary layer. *Bound.-Layer Meteor.,* **105,** 305–328.

Desjardins, R. L., J. I. MacPherson, P. H. Schuepp, and F. Karanja, 1989: An evaluation of aircraft flux measurements of CO_2, water vapor and sensible heat. *Bound.-Layer Meteor.,* **47,** 55–69.

Friehe, C. A., and Coauthors, 1991: Air-sea fluxes and surface layer turbulence around a sea surface temperature front. *J. Geophys. Res.,* **96** (C5), 8593–8609.

Fujita, T., 1963: Analytical mesometeorology: A review. *Severe Local Storms, Meteor. Monogr.,* No. 27, Amer. Meteor. Soc., 77–125.

Garratt, J. R., 1992: *The Atmospheric Boundary Layer.* Cambridge Atmospheric and Space Science Series, Cambridge University Press, 316 pp.

Haltiner, G. J., and R. T. Williams, 1990: *Numerical Prediction and Dynamic Meteorology.* Wiley and Sons, 477 pp.

Holton, J. R., 1979: *An Introduction to Dynamic Meteorology.* Academic Press, 391 pp.

Horst, T. W., and S. P. Oncley, 2006: Corrections to inertial-range power spectra measured by CSAT3 and Solent sonic anemometers, 1. Path-averaging errors. *Bound.-Layer Meteor.,* **119,** 375–395.

Howell, J. F., and J. Sun, 1999: Surface-layer fluxes in stable conditions. *Bound.-Layer Meteor.,* **90,** 495–520.

Hoxit, L. R., 1974: Planetary boundary layer winds in baroclinic conditions. *J. Atmos. Sci.,* **31,** 1003–1020.

Jeffreys, H., 1922: On the dynamics of wind. *Quart. J. Roy. Meteor. Soc.,* **48,** 29–46.

Johnson, R. H., 2001: Surface mesohighs and mesolows. *Bull. Amer. Meteor. Soc.,* **82,** 13–31.

Johnson, W. B., 1966: The ''geotriptic'' wind. *Bull. Amer. Meteor. Soc.,* **47,** 982.

LeMone, M. A., G. M. Barnes, J. C. Fankhauser, and L. F. Tarleton, 1988: Perturbation pressure fields measured by aircraft around the cloud-base updraft of deep convective clouds. *Mon. Wea. Rev.,* **116,** 313–327.

Macklin, S. A., G. M. Lackmann, and J. Gray, 1988: Offshore-directed winds in the vicinity of Prince William Sound, Alaska. *Mon. Wea. Rev.,* **116,** 1289–1301.

Mahrt, L., 2009: Characteristics of submeso winds in the stable boundary layer. *Bound.-Layer Meteor.,* **130,** 1–14.

——, 2010: Computing turbulent fluxes near the surface: Needed improvements. *Agric. For. Meteor.,* **150,** 501–509.

——, C. Thomas, S. Richardson, N. Seaman, D. Stauffer, and M. Zeeman, 2012: Non-stationary generation of weak turbulence for very stable and weak-wind conditions. *Bound.-Layer Meteor.,* **147,** 179–199, doi:10.1007/s10546-012-9782-x.

Mass, C. F., and W. J. Steenburgh, 2000: An observational and numerical study of an orographically trapped wind reversal along the west coast of the United States. *Mon. Wea. Rev.,* **128,** 2363–2395.

McKendry, I. G., A. P. Sturman, and I. F. Owens, 1986: A study of interacting multi-scale wind systems, Canterbury Plains, New Zealand. *Meteor. Atmos. Phys.,* **35,** 242–252.

Nadolski, V. L., 1998: Automated Surface Observing System (ASOS) user's guide. National Oceanic and Atmospheric

Administration, Department of Defense, Federal Aviation Administration, United States Navy, 20 pp.

Nishiyama, R. T., and A. J. Bedard Jr., 1991: A "Quad-Disc" static pressure probe for measuring in adverse atmospheres: With a comparative review of static pressure probe designs. *Rev. Sci. Instrum.,* **62,** 2193–2204.

Parish, T. R., and K. T. Waight III, 1987: The forcing of Antarctic katabatic winds. *Mon. Wea. Rev.,* **115,** 2214–2226.

——, M. D. Burkhart, and A. R. Rodi, 2007: Determination of the horizontal pressure gradient force using global positioning system on board an instrumented aircraft. *J. Atmos. Oceanic Technol.,* **24,** 521–528.

Pennell, W. T., and M. A. LeMone, 1974: An experimental study of turbulence structure in the fair-weather trade wind boundary layer. *J. Atmos. Sci.,* **31,** 1308–1323.

Poulos, G. S., and Coauthors, 2002: CASES-99—A comprehensive investigation of the stable nocturnal boundary layer. *Bull. Amer. Meteor. Soc.,* **83,** 555–581.

Raymond, W. H., 1993: Moist wind relationships. *Mon. Wea. Rev.,* **121,** 1992–2003.

Saucier, W. J., 1955: *Principles of Meteorological Analysis.* The University of Chicago Press, 438 pp.

Schaefer, J. T., and C. A. Doswell III, 1980: The theory and practical application of antitriptic balance. *Mon. Wea. Rev.,* **108,** 746–756.

Schlichting, H., and K. Gersten, 2000: *Boundary-Layer Theory.* Springer, 801 pp.

Sheppard, P. A., H. Charnock, and J. R. D. Francis, 1952: Observations of the westerlies over the sea. *Quart. J. Roy. Meteor. Soc.,* **78,** 563–582.

Staebler, R. M., and D. R. Fitzjarrald, 2004: Observing subcanopy CO_2 advection. *Agric. For. Meteor.,* **122,** 139–156.

——, and ——, 2005: Measuring canopy structure and the kinematics of subcanopy flows in two forests. *J. Appl. Meteor.,* **44,** 1161–1179.

Sun, J., 2011: Vertical variations of the mixing lengths during CASES-99. *J. Appl. Meteor. Climatol.,* **50,** 2030–2041.

——, and Coauthors, 2002: Intermittent turbulence associated with a density current passage in the stable boundary layer. *Bound.-Layer Meteor.,* **105,** 199–219.

——, L. Mahrt, R. M. Banta, and Y. L. Pichugina, 2012: Turbulence regimes and turbulence intermittency in the stable boundary layer during CASES-99. *J. Atmos. Sci.,* **69,** 338–351.

Van de Wiel, B. J. H., A. F. Moene, H. J. J. Jonker, P. Baas, S. Basu, J. M. M. Donda, J. Sun, and A. A. M. Holtslag, 2012: The minimum wind speed for sustainable turbulence in the nocturnal boundary layer. *J. Atmos. Sci.,* **69,** 3116–3127.

Vescio, M. D., and R. H. Johnson, 1992: The surface-wind response to transient mesoscale pressure fields associated with squall lines. *Mon. Wea. Rev.,* **120,** 1837–1850.

Vickers, D., and L. Mahrt, 2003: The cospectral gap and turbulent flux calculations. *J. Atmos. Oceanic Technol.,* **20,** 660–672.

——, and ——, 2006: A solution for flux contamination by mesoscale motions with very weak turbulence. *Bound.-Layer Meteor.,* **118,** 431–447.

Wilczak, J. M., and A. J. Bedard Jr., 2004: A new turbulence microbarometer and its evaluation using the budget of horizontal heat flux. *J. Atmos. Oceanic Technol.,* **21,** 1170–1181.